MITSUBISHI ELECTRIC RESEARCH LABORATORIES
https://www.merl.com

Static Eccentricity Fault Detection for PSH-type Induction Motors Considering High-order Air Gap Permeance Harmonics

Zhou, Lei; Wang, Bingnan; Lin, Chungwei; Miyoshi, Masahito; Inoue, hiroshi

TR2021-051 May 18, 2021

Abstract

Diagnosis of static eccentricity (SE) faultfor induction motors (IMs) is essential for the quality control of the machines, especially during their manufacturing process. Principal slot harmonic (PSH) type IMs have special combinations of rotor bar number and pole pair number, and it has been shown in previous works that conventional methods cannot effectively detect SE fault for these machines. Aiming at finding an effective approach for the SE fault detection for PSHtype IMs, this paper presents an analysis of SE-induced line currents in IMs with the higher-order harmonics of the air gap permeance considered. The analysis reveals that the second-order harmonic in the air gap permeance can induce SE-level-related signals in the line current of PSH-type three-phase IMs. The generation mechanism of the signature current signal is validated by simulations with an analytical IM model and a timestepping finite element model. The signature signal in the motor's current discussed in this paper provides a new method for quantitative detection of SE fault for PSH-type IMs.

IEEE International Electric Machine & Drives Conference (IEMDC)

Mitsubishi Electric Research Laboratories, Inc.
201 Broadway, Cambridge, Massachusetts 02139

Static Eccentricity Fault Detection for PSH-type Induction Motors Considering High-order Air Gap Permeance Harmonics

Lei Zhou
Dept. of Mechanical Engineering
The University of Texas at Austin
lzhou@utexas.edu

Bingnan Wang
Mitsubishi Electric Research Labs
Cambridge, USA
bwang@merl.com

Chungwei Lin
Mitsubishi Electric Research Labs
Cambridge, USA
clin@merl.com

Hiroshi Inoue
Advanced R&D Center
Mitsubishi Electric Corp.
Inoue.Hiroshi@cw.Mitsubishi-Electric.co.jp

Masahito Miyoshi
Advanced R&D Center
Mitsubishi Electric Corp.
Miyoshi.Masahito@ay.Mitsubishi-Electric.co.jp

***Abstract*—Diagnosis of static eccentricity (SE) fault for induction motors (IMs) is essential for the quality control of the machines, especially during their manufacturing process. Principal slot harmonic (PSH) type IMs have special combinations of rotor bar number and pole pair number, and it has been shown in previous works that conventional methods cannot effectively detect SE fault for these machines. Aiming at finding an effective approach for the SE fault detection for PSH-type IMs, this paper presents an analysis of SE-induced line currents in IMs with the higher-order harmonics of the air gap permeance considered. The analysis reveals that the second-order harmonic in the air gap permeance can induce SE-level-related signals in the line current of PSH-type three-phase IMs. The generation mechanism of the signature current signal is validated by simulations with an analytical IM model and a time-stepping finite element model. The signature signal in the motor's current discussed in this paper provides a new method for quantitative detection of SE fault for PSH-type IMs.**

***Index Terms*—Induction motor, fault detection, static eccentricity, motor current signature analysis**

I. Introduction

Eccentricity is a type of motor fault caused by non-uniform air gap between the stator bore and the rotor. There are three types of motor eccentricity fault: the static eccentricity (SE), the dynamic eccentricity (DE), and the mixed eccentricity (ME). Figure 1 shows a diagram for the three types of eccentricity. Here, the point O_w is the center of rotation, O_s is the center of the stator bore, and O_r is the center of rotor. When the three points coincide, the motor is healthy with no eccentricity fault, as shown in Fig. 1a. In the case of SE, the points O_r and O_w coincide, but are having an offset from the center of the stator bore O_s, as shown in Fig. 1b. When under DE fault, the rotor's center of rotation O_w is aligned with the stator center O_s, but the rotor center O_r is orbiting around the point O_w, as shown in Fig. 1c. A mixture of both static and dynamic eccentricity is called ME, where the points O_r, O_s, and O_w are not aligned with one another, as shown in Fig. 1d. Typically the SE fault of motors is created during the manufacturing process due to the ovality of the stator bore and the misalignment of bearings. The detection of SE fault of machines at an early stage is essential, as it can evolve into severe ME over the motor's operation due to the unbalanced magnetic pull, and lead to the breakdown of the machine.

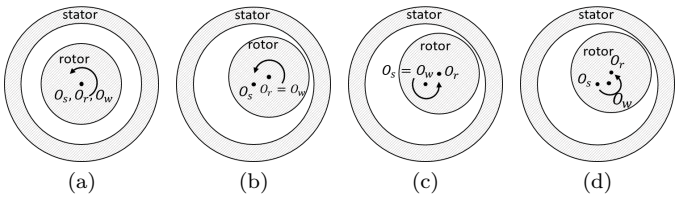

Fig. 1. Diagram of different types of eccentricity fault. O_s: stator center. O_r: rotor center. O_w: center of rotation. (a) Healthy motor. (b) Static eccentricity. (c) Dynamic eccentricity. (d) Mixed eccentricity.

Throughout the years, a number of methods have been proposed for the SE fault detection [2], [5]–[8]. The motor current signature analysis (MCSA) is one of the most widely used method due to its advantages of low-cost, reliability and simplicity, and the fact that no additional sensor is required to attach to the motor. For most IMs with SE or DE fault, the signature frequency in the current signal is [1]

$$f_h = \big((kR \pm n_d)\frac{1-s}{p} \pm \nu\big) f, \tag{1}$$

where f is the fundamental frequency, R is the number of rotor slots, s is the slip, p is number of pole pairs, k is any positive integer, n_d is the eccentricity order, and ν is the order of stator time harmonics. Note that the frequency in (1) coincide with the motor's principal slot harmonic

TABLE I
STATIC ECCENTRICITY DETECTION BASED ON EXISTING THEORY AND THE PROPOSED THEORY.

Static eccentricity detection method	Non-PSH IM		PSH IM
	Case A: $R = 2p[3(m \pm q) \pm r] \pm 1$	Case B: $R = 2p[3(m \pm q) \pm r] \pm 2$	Case C: $R = 2p[3(m \pm q) \pm r]$
Existing methods considering only fundamental harmonic of air gap permeance [1]–[4]	Large SE signature signal	Small SE signature signal	Irreverent to SE: **Not Detectable**
Proposed method considering 2nd-order harmonic air gap permeance	Large SE signature signal	Small SE signature signal	Small SE signature signal at secondary PSH frequency: **Detectable**

(PSH) signals under $k = \nu = 1$.

The signature current signals at frequencies in (1) are effective for most three-phase IMs for eccentricity fault detection. However, it has been shown in Ref. [1] that when an IM has a combination of pole pair number p and rotor slot number R that satisfies

$$R = 2p[3(m \pm q) \pm r], \tag{2}$$

where $m \pm q = 0, 1, 2, ...$, and r = 0 or 1, the current at the signature frequencies (1) has been reported to be irrelevant to the machine's SE faults. IMs satisfying (2) are called PSH-type motors. For this group of IMs, the PSH current signals are generated under both healthy and eccentric conditions, and their amplitudes do not show significant dependency on eccentricity level. This statement has been validated via model-based simulations in Ref. [1], and it is widely believed that there is no effective MCSA-based SE fault detection method for PSH-type IMs [2]–[4].

The objective of this paper is to thoroughly investigate the PSH-type induction machines, as a means to provide a new and effective MCSA-based method for SE fault detection for three-phase PSH-type induction motors. Prior work Ref. [1] considers only the constant and the fundamental harmonic terms of the air gap permeance, which does not capture the eccentricity-related signals generated due to the higher-order air gap permeance harmonics. In this paper, we first present a detailed analysis for three-phase IMs with the high-order harmonics of air gap permeance considered. Our analysis reveals that the second-order harmonic of the air gap permeance generates a signature current signal for SE fault in the PSH-type IM's stator current, which potentially can be used for the SE fault detection for these motors. Table I presents the categorization of the IMs and its impact on the SE fault detection, as well as the major differences between the existing theory [1]–[4] and the proposed analysis. An analytical IM model based on the modified winding function method (MWFM) is used to validate the theoretical analysis, and time-stepping finite element simulations are used to show the effectiveness of the proposed SE fault detection method.

The rest of this paper is organized as follows. Section II presents an analysis for the motor flux harmonics and the motor line current signals caused by SE fault in three-phase IM motors. The higher-order harmonics of the air gap permeance are considered in this analysis. The new MCSA-based SE fault detection method for PSH-type IMs is also proposed in Section II. Section III presents an analytical IM model and its simulation results, and time-stepping finite element simulation is used to validate the proposed method. Conclusions and the suggested future work are presented in Section IV.

II. Analysis of Static-Eccentricity-Related Current Signals

This section presents an analysis for the IM's air gap flux and line current signals generated by SE fault. This analysis contrasts reference [1] in that we consider the high-order harmonics of the air gap permeance in the derivation. These air gap permeance harmonics can generate SE-related signature signals in the line current of the PSH-type IMs, which provides a new method for the SE fault detection for these machines. We next present an analysis for the air gap flux harmonics induced by the rotor's slotting effect, which are the source of the PSH current signals. After this we discuss the generation of induced stator line current due to these air gap fluxes.

A. Slots-induced Air Gap Flux Harmonics

In an IM, the fundamental harmonic of the stator-generated magnetomotive-force (MMF) is

$$\mathcal{F}_s = A\cos(p\phi - \omega t), \tag{3}$$

where p is the number of pole pairs, ω is the supply angular frequency, ϕ is the angular coordinate in a stator-fixed reference frame, and A is the amplitude of the fundamental harmonic of stator MMF.

When the motor is having a SE fault, the air gap length distribution is

$$g(\phi) = g_0(K_{cs} - \delta_{SE}\cos\phi), \tag{4}$$

where g_0 is the nominal air gap length, K_{cs} is the Carter's coefficient to correct the air gap length for the slotting effects, and $\delta_{SE} \in [0, 1]$ is the SE level. The air gap permeance of the motor is defined as $P_g = \mu_0/g$. In many

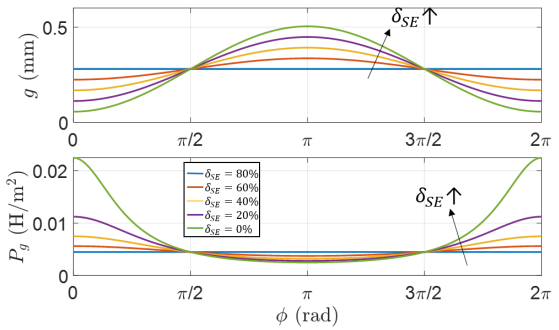

(a)

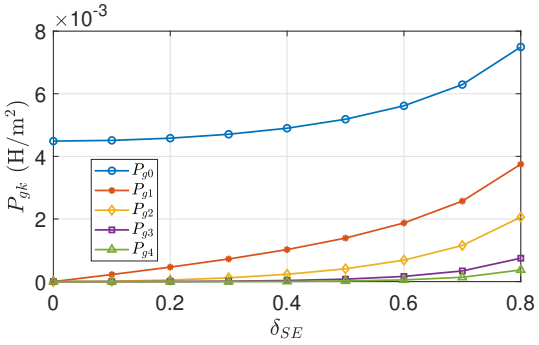

(b)

Fig. 2. (a) Air gap length g and air gap permeance P_g as functions of mechanical angle ϕ under varying δ_{SE}. (b) Values of first four Fourier coefficients of air gap permeance under varying static eccentricity levels.

references on IM eccentricity fault detection [1], [6], [9], the air gap permeance is typically described as

$$\text{Model I: } P_g \approx P_{g0} + P_{g1}\cos\phi, \tag{5}$$

where only the constant term and the fundamental harmonic of the air gap permanence are considered. However, the full Fourier series representing P_g is

$$\text{Model II: } P_g = P_{g0} + \sum_{k=1}^{\infty} P_{gk}\cos(k\phi). \tag{6}$$

We will refer (5) and (6) as permeance Model I and II respectively in the paper. Figure 2 shows the air gap length, permeance, and the value of first five terms of P_{gk} for a typical IM under varying SE level. It can be observed in Fig. 2b that P_{g0}, P_{g1}, and P_{g2} have relatively strong dependency with respect to δ_{SE}. This observation shows that the conventionally assumed permeance Model I in prior works may not be accurate enough to capture all signature signals caused by SE faults.

The stator MMF in (3) acting on the air gap permeance (6) and produces an air gap flux distribution as

$$\begin{aligned}\Phi^s_{g1} &= \mathcal{F}_s P_g = A\cos(p\phi-\omega t)\big(P_{g0}+\sum_{k=1}^{\infty}P_{gk}\cos(k\phi)\big) \\ &= AP_{g0}\cos(p\phi-\omega t) + \sum_{k=1}^{\infty}\frac{AP_{gk}}{2}\cos\big((p\pm k)\phi-\omega t\big).\end{aligned} \tag{7}$$

Transforming this stator-generated flux (7) into the rotor-fixed coordinate via $\phi = \phi' + \omega_r t$, where ϕ' is the angular coordinate in the rotor-fixed frame, we have

$$\begin{aligned}\Phi^r_{g1} =& AP_{g0}\cos(p\phi' + p\omega_r t - \omega t) \\ &+ \sum_{k=1}^{\infty}\frac{AP_{gk}}{2}\cos\big((p\pm k)\phi' + (p\pm k)\omega_r t - \omega t\big).\end{aligned} \tag{8}$$

The stator-generated air gap flux (8) induces currents in the rotor bars, which generates a rotor MMF. Aside from the harmonics that have the same wavelength as the stator-generated air gap flux in (8), additional rotor slot harmonics are generated. Such rotor slot harmonics can be visualized as the original waveforms sampled by the discrete rotor bars, i.e. a $\cos(R\phi')$ term is multiplied to the original flux harmonic. Such rotor slot harmonic MMF can be written as

$$\begin{aligned}\mathcal{F}^r_{nslot} =& A_0^{slot}P_{g0}\cos\big(R\phi' + \nu_0(p\phi' + p\omega_r t - \omega t) + \phi_0\big) \\ &+ \sum_{k=1}^{\infty}A_k^{slot}P_{gk}\cos\Big(R\phi' + \nu_k\big((p\pm k)\phi' \\ &\qquad + (p\pm k)\omega_r t - \omega t\big) + \phi_k\Big),\end{aligned} \tag{9}$$

where $\nu_0 = \pm 1$, and $\nu_k = \pm 1$. Transforming (9) back to the stator-fixed coordinate via $\phi' = \phi - \omega_r t$ yields

$$\begin{aligned}\mathcal{F}^s_{nslot} =& A_0^{slot}P_{g0}\cos\big((R+\nu_0 p)\phi - R\omega_r t - \nu_0\omega t + \phi_0\big) \\ &+ \sum_{k=1}^{\infty}A_k^{slot}P_{gk}\cos\Big(\big(R+\nu_k(p\pm k)\big)\phi \\ &\qquad - R\omega_r t - \nu_k\omega t + \phi_k\Big).\end{aligned} \tag{10}$$

The rotor slot harmonic MMF (10) acts across the gap again and generates an air gap flux as

$$\Phi^s_{g2} = \mathcal{F}^s_{nslot}P_g. \tag{11}$$

Substituting (6) and (10) into (11), we can calculate the rotor-generated air gap flux that has several different harmonics, particularly including the following terms:

$$\begin{aligned}\Phi^s_{g2,00} =& A_0^{slot}P_{g0}^2\cdot \\ &\cos\big((R+\nu_0 p)\phi - R\omega_r t - \nu_0\omega t + \phi_{00}\big),\end{aligned} \tag{12}$$

$$\begin{aligned}\Phi^s_{g2,0j} =& \sum_{j=1}^{\infty}\frac{A_0^{slot}P_{g0}P_{gj}}{2}\cdot \\ &\cos\big((R+\nu_0 p+\nu_j j)\phi - R\omega_r t - \nu_0\omega t + \phi_{0j}\big),\end{aligned} \tag{13}$$

$$\begin{aligned}\Phi^s_{g2,k0} =& \sum_{j=1}^{\infty}A_k^{slot}P_{gk}P_{g0}\cdot \\ &\cos\big((R+\nu_k p+\nu_{k1}k)\phi - R\omega_r t - \nu_k\omega t + \phi_{k0}\big),\end{aligned} \tag{14}$$

$$\begin{aligned}\Phi^s_{g2,jk} =& \sum_{j=1}^{\infty}\sum_{k=1}^{\infty}\frac{A_k^{slot}P_{gj}P_{gk}}{2}\cdot \\ &\cos\big((R+\nu_k p+\nu_{k1}k+\nu_j j)\phi \\ &\qquad - R\omega_r t - \nu_k\omega t + \phi_{jk}\big),\end{aligned} \tag{15}$$

where $\nu_j = \pm 1$, $\nu_{k1} = \pm 1$. Note that all these air gap flux harmonics have the same frequency of

$$f_{PSH} = \frac{1}{2\pi}(R\omega_r - \nu_i\omega) = (R\frac{1-s}{p} - \nu_i)f, \tag{16}$$

where $\nu_i = \pm 1$ represents ν_0 or ν_k. Also note that the (12) term exists no matter the motor is healthy or under eccentricity fault; terms (13)-(15) exist only when the motor is having SE faults. When only considering the terms with $k = j = 1$, this result matches with the analysis assuming sinusoidal air gap permeance in [1].

B. Current Signature Signal Generation

This section discusses the generation of SE-related current signature signals due to the air gap fluxes (12)-(15). Note that the frequency of the SE-generated current signal is always at PSH frequency shown in (16).

In order to generate line current signals in the motor windings, the air gap flux needs to induce none-zero-sequence voltage in the stator windings. Such induced voltage can be calculated via

$$\begin{aligned} v_{si}(t) &= -\frac{\mathrm{d}}{\mathrm{d}t}\lambda_i(t) \\ &= -\frac{\mathrm{d}}{\mathrm{d}t}\int_0^{2\pi} N_i(\phi)\Phi^s_{g2}(\phi, t)\mathrm{d}\phi, \end{aligned} \tag{17}$$

where N_i is the stator winding distribution function, and $i = 0, 1, 2$ for phases u, v, and w, respectively. For a three-phase IM with pole-pair number p, the stator winding distribution function N_i is

$$N_i(\phi) = \sum_{j=1}^{\infty} N_i^j \cos\left(j(p\phi - \frac{2\pi i}{3})\right), \tag{18}$$

where N_i^j is the amplitude of the j-th harmonic of the stator winding function N_i, and j is an odd number. Note that the triplen harmonics of the winding distribution functions are having the same phase due to the three-phase symmetry.

Assume a certain air gap flux harmonic is having a pole pair number p_Φ, for this flux to generate non-zero-sequence induced voltage, we require that p_Φ is not divisible by $2p$ or $3p$, i.e.

$$p_\Phi/p = 6m \pm 1, \tag{19}$$

where m = 0, 1, 2, ... Equation (19) is the condition for an air gap flux to induce line current in the motor windings.

We next discuss the air gap fluxes (12)-(15) and the induced SE-related line currents.

(I) Air gap flux (12)**:** The air gap flux term $\Phi^s_{g2,00}$ in (12) exists under both healthy and eccentric conditions, and it can generate PSH signals when the motor has $\big(R + \nu_0 p\big)/p = 6m \pm 1$, i.e.

$$R = p(6m \pm 1) - \nu_0 p, \tag{20}$$

where $m = 0, 1, 2, ...$ Considering $\nu_0 = \pm 1$, this condition is equivalent to (2) in [1]. For a specific motor, only one PSH signal can be generated. For example, a motor with $R = 28$ and $p = 2$ satisfies (20) when $\nu_0 = -1$, and the corresponding PSH signal frequency is at $\omega_{PSH} = R\omega_r - \omega$, or $f_{PSH} = (R\frac{1-s}{p} - 1)f$. The condition (20) cannot be satisfied with $\nu_0 = 1$, and there is no PSH signal at $(R\frac{1-s}{p} + 1)f$.

(II) Air gap fluxes (13) **and** (14)**:** The air gap flux terms (13) and (14) are having similar forms. Here we discuss the air gap flux $\Phi^s_{g2,0j}$ in (13); the air gap flux (14) can be analyzed in a similar manner. The air gap flux (13) can generate induced line current when the motor's parameters satisfy $(R + \nu_0 p + \nu_j j)/p = 6m \pm 1$, i.e.

$$R = p(6m \pm 1) - \nu_0 p - \nu_j j, \tag{21}$$

where $m = 0, 1, 2, ...$ When $j = 1$, the induced current signal demonstrates a relatively strong static-eccentricity-dependent signal at frequency (16), and the current amplitude is proportional to $P_{g0}P_{g1}$. When $j = 2$, an eccentricity-related line current can also be induced, with the signal's amplitude largely proportional to $P_{g0}P_{g2}$. For a PSH-type motor, no SE signature signals can be generated by this air gap flux component (13). For example, for an IM with $R = 28$ and $p = 2$, selecting different combinations of ν_0, ν_j, and $j = 1$ or 2 cannot satisfy the condition in (21). This conclusion is consistent with the previous analysis in [1].

(III) Air gap flux (15)**:** The flux $\Phi^s_{g2,jk}$ in (15) can generate induced line current for the motor when $(R + \nu_k p + \nu_k k + \nu_j j)/p = 6m \pm 1$, i.e.

$$R = p(6m \pm 1) - \nu_k p - \nu_k k - \nu_j j, \tag{22}$$

where $m = 0, 1, 2, ...$, $\nu_k = \pm 1$, $\nu_j = \pm 1$. When $j = 1$, $k = 1$, the induced current signal amplitude is proportional to P^2_{g1}, which is largely quadratic with respect to δ_{SE}. When $j = 2$, $k = 2$, the induced line current is proportional to P^2_{g2}. Although the induced signal under this condition is not as strong as the other cases, this flux produces an opportunity of the usage of MCSA for SE detection for PSH-type machines. For example, for an IM with $R = 28$ and $p = 2$, the condition (22) can be satisfied with $k = j = 2$ and $\nu_k = \nu_j = 1$, and the generated SE-related line current signal at the frequency $(R\frac{1-s}{p} + 1)f$. This signal can be used for the detection of SE level for PSH-type induction machines.

III. Simulation Validations

This section presents the simulation for the proposed SE detection method for PSH-type IMs. A 0.75 kW, three-phase, 2-pole-pair squirrel-cage IM is evaluated in this work. The motor has 36 stator slots and 28 rotor slots. The three-phase stator windings are having a Y-connection. The RMS line-to-line voltage and frequency are 196 V and 60 Hz, respectively. Table II shows the motor design parameters. This motor belongs to the PSH-type IM category, since its number of rotor bars and number of pole pairs satisfy the relationship shown in

TABLE II
PARAMETERS OF THE EVALUATED PSH-TYPE INDUCTION MOTOR

Parameter	Value
Number of pole pairs	2
Number of bars	28
Number of stator slots	36
Number of turns per slot	37
Nominal air gap length	0.28 mm
Air gap radius	41.6 mm
Stack length	80 mm
Carter's coefficient	1.38

(2). Conventional MCSA-based methods cannot detect SE fault for this machine. We next discuss the simulation with an analytical model based on the modified winding function method (MWFM) in Section III-A and III-B. After that we present the evaluation using time-stepping FEM simulation in Section III-C.

A. Analytical Induction Motor Model

This section presents the analytical model and simulation results for IM. We first briefly present the multiple coupled circuit model for the Y-connected three-phase IM. The stator voltage dynamics and the stator flux linkage are

$$V_s = R_s I_s + \frac{\mathrm{d}}{\mathrm{d}t}\Lambda_s, \tag{23}$$

$$\Lambda_s = L_{ss} I_s + L_{sr} I_r, \tag{24}$$

where $V_s = [v_{s1}, v_{s2}, v_{s3}]^\top$ is the stator voltage, Λ_s is the stator flux linkage, $I_s = [i_{s1}, i_{s2}, i_{s3}]^\top$ is the stator current, $I_r = [i_{r1}, i_{r2}, ..., i_{rR}, i_e]^\top$ is the vector for rotor loop currents and the end ring current. R_s is a 3×3 is the stator resistance matrix, L_{ss} is a 3×3 stator inductance matrix, and L_{sr} is a $3 \times (R+1)$ matrix of the mutual inductance between stator phases and rotor loops. The voltage dynamics of the rotor loops and the rotor flux are

$$V_r = R_r I_r + \frac{\mathrm{d}}{\mathrm{d}t}\Lambda_r, \tag{25}$$

$$\Lambda_r = L_{rs} I_s + L_{rr} I_r, \tag{26}$$

where $V_r = [0, 0, ..., 0]^\top$ for squirrel cage rotors, $L_{rs} = L_{sr}^\top$, and L_{rr} is an $(R+1) \times (R+1)$ matrix of the rotor self inductance.

For a three-phase IM with Y-connection, the input signals are the line-to-line voltages. Transforming the stator voltage equation (23) into line-to-line voltage input we have

$$V_{sl-l} = \begin{bmatrix} v_{s1} - v_{s2} \\ v_{s2} - v_{s1} \\ v_{s3} - v_{s1} \end{bmatrix} = \begin{bmatrix} r_s & -r_s & 0 \\ 0 & r_s & -r_s \\ -r_s & 0 & r_s \end{bmatrix} I_s + \frac{\mathrm{d}}{\mathrm{d}t}\Lambda_{sl-l}, \tag{27}$$

where $\Lambda_{sl-l} = [\lambda_{s1} - \lambda_{s2}, \lambda_{s2} - \lambda_{s3}, \lambda_{s3} - \lambda_{s1}]^\top$.

The motor's stator has Y-connected winding and no neutral line, forcing the summation of three line currents to be zero. Hence we have

$$\begin{bmatrix} \lambda_{s1} - \lambda_{s2} \\ \lambda_{s2} - \lambda_{s3} \\ 0 \end{bmatrix} = \begin{bmatrix} L_{s11} - L_{s21} & L_{s12} - L_{s22} & L_{s13} - L_{s23} \\ L_{s21} - L_{s31} & L_{s22} - L_{s32} & L_{s23} - L_{s33} \\ 1 & 1 & 1 \end{bmatrix} I_s + \begin{bmatrix} L_{sr1} - L_{sr2} \\ L_{sr2} - L_{sr3} \\ 0 \end{bmatrix} I_r. \tag{28}$$

Equations (25)-(28) fully describe the line-to-line electrical dynamics of the IM. This treatment of the Y-connection follows reference [10]. The torque of the motor is

$$T_e = \frac{1}{2} I_s^\top \frac{\partial L_{ss}}{\partial \theta_r} I_s + I_s^\top \frac{\partial L_{sr}}{\partial \theta_r} I_r + \frac{1}{2} I_r^\top \frac{\partial L_{rr}}{\partial \theta_r} I_r, \tag{29}$$

where θ_r is the rotor's mechanical angle. The mechanical dynamics of the motor is

$$\frac{\mathrm{d}}{\mathrm{d}t}\omega_r = \frac{1}{J}(T_e - T_L), \tag{30}$$

$$\frac{\mathrm{d}}{\mathrm{d}t}\theta_r = \omega_r, \tag{31}$$

where ω_r is the mechanical speed, T_L is the load torque, and J is the rotor inertia.

The MWFM [11] is used to calculate the motor's inductance matrices. The inductance between winding i and winding j can be calculated as

$$L_{ij}(\theta_r) = lr \int_0^{2\pi} n_i(\theta_r, \phi) M_j(\theta_r, \phi) P_g(\theta_r, \phi) \mathrm{d}\phi, \tag{32}$$

where r and l are the air gap radius and motor axial length, respectively, $n_i(\theta_r, \phi)$ is the winding turns function for winding i. $M_j(\theta_r, \phi)$ is the modified winding function for winding j, which is calculated as

$$M(\phi, \theta_r) = n(\phi, \theta_r) - \Big\langle M(\theta_r) \Big\rangle, \tag{33}$$

where

$$\Big\langle M(\theta_r) \Big\rangle = \frac{1}{2\pi \langle g^{-1}(\theta_r, \phi) \rangle} \int_0^{2\pi} n(\phi, \theta_r) g^{-1}(\theta_r, \phi) \mathrm{d}\phi, \tag{34}$$

$$\Big\langle g^{-1}(\theta_r, \phi) \Big\rangle = \frac{1}{2\pi} \int_0^{2\pi} g^{-1}(\theta_r, \phi) \mathrm{d}\phi. \tag{35}$$

B. Analytical Model Simulation Results

The motor's dynamics are simulated using an analytical coupled circuit model with the MWFM [6], [9]. The load torque T_L is set to zero, and the supply frequency is 60 Hz. Under these conditions, the PSH frequency is 780 Hz, and the expected signature signal of SE fault due to the second-order harmonic of the air gap permeance is at 900 Hz. In this work, the two air gap permeance Model I (equation (5)) and Model II (equation (6)) are used to evaluate the effect of the higher-order terms of P_g.

Figure 3a and 3b show the simulated current spectrum around 780 Hz and 900 Hz under varying SE levels, where Fig. 3a is obtained with air gap permeance Model I, and

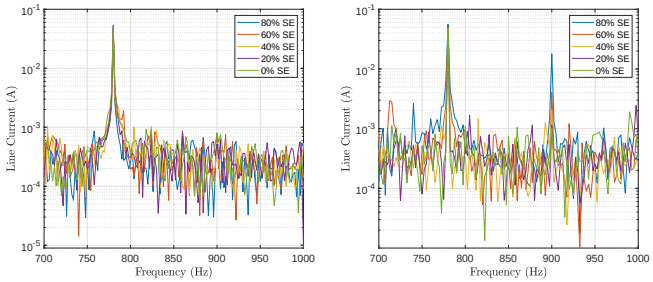

(a) (b)

Fig. 3. Analytical IM model simulated motor line current spectrum under varying static eccentricity levels. (a) Air gap permeance model I. (a) Air gap permeance model II.

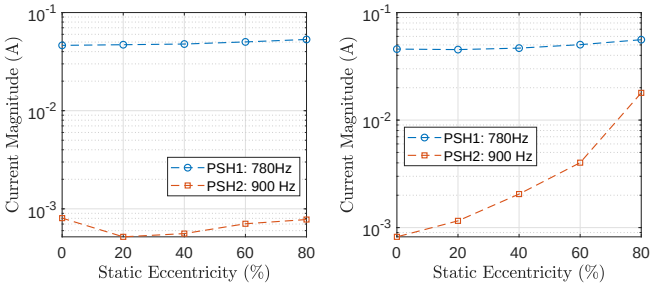

(a) (b)

Fig. 4. Amplitude of PSH currents simulated by analytical IM model. (a) Air gap permeance model I. (a) Air gap permeance model II.

Fig. 3b is calculated using air gap permeance Model II. Both current spectrum data demonstrate peak at 780 Hz, which is the PSH frequency of the motor when $f = 60$ Hz and $s = 0$. Figure 3b demonstrates an additional 900 Hz signal with its amplitude positively correlated with the level of SE fault. Figure 4 shows the amplitude of the 780 Hz and 900 Hz current signals with respect to eccentricity level. The data in Fig. 4a agrees with the simulation results presented in recent reference [12]. This comparison shows that it is the difference in the air gap permeance model that causes the 900 Hz signal in the line current.

C. Finite Element Simulations

The same 0.75 kW IM is also simulated via time-stepping finite element method under different static eccentricity levels. Here the FEM package Ansys Maxwell is used. The motor is simulated under no-load condition. Here we limited the level of eccentricity up to 40% to avoid signals generated by mesh-induced asymmetry. Figure 5 shows the spectra of the FEM-simulated single-phase and line-to-line induced voltages, respectively.

Fig. 5 shows the FEM simulated phase u line current around the PSH signals, where Fig. 5a shows the current spectrum, and Fig. 5b shows the current magnitude of the two PSH frequencies. It can be observed that FEM-simulated motor line current has peaks appearing at both 780 Hz and 900 Hz as expected. The magnitude of the 900 Hz signal is positively correlated to the level of SE,

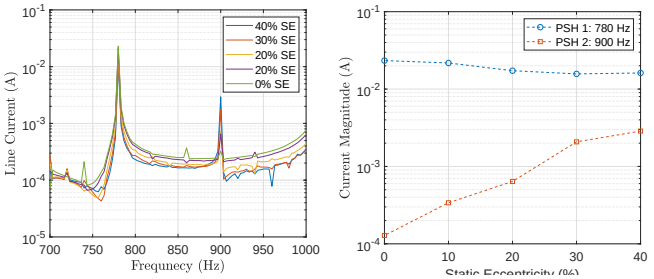

(a) (b)

Fig. 5. FEM simulated line current under varying static eccentricity levels. (a) Current spectrum. (b) PSH current amplitude.

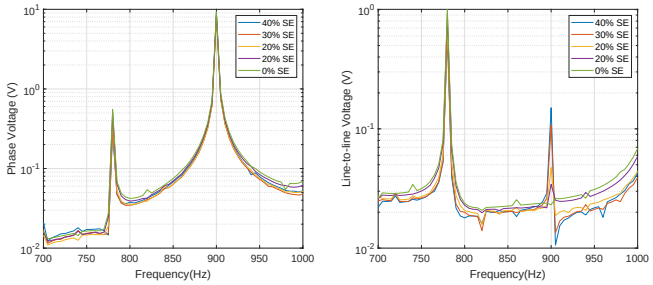

(a) (b)

Fig. 6. FEM simulated motor induced voltage signals under varying static eccentricity levels. (a) Phase A voltage. (b) Line-to-line voltage between phase A and phase B.

which resembles the signal shown in Fig. 4b. This observation validates the analytical model for IM considering the higher-order harmonics of air gap permeance, and also confirms that the secondary PSH current signal (at 900 Hz for the motor being evaluated) can be used for SE detection.

We next evaluated the induced voltage signals in the IM under different SE levels. Fig. 6 shows the FEA-simulated single-phase voltage and the line-to-line voltage. The 900 Hz voltage has a large amplitude in the single-phase voltage in Fig. 6, and is having a relatively small amplitude in the line-to-line voltage in Fig. 6b. This is because the 900 Hz voltage is primarily zero-sequence due to both slot harmonics and the 15th-harmonic of supply, which agrees with our analysis based on analytical model. The amplitude of the line-to-line voltage at 900 Hz varies with the SE level, which generates the SE-dependent line current signal shown in Fig. 5.

IV. Conclusions and Future Work

This paper presented an analysis for IM with static eccentricity fault and showed that the second-order harmonic of the air gap permeance can induce an SE-dependent signal in the motor's line current for PSH-type IM. Analytical and finite element models validated the analysis, showing the correlation between the amplitude of the secondary PSH current signal and the SE level. This

provides a new method for PSH-type IM's SE detection based on MCSA, which has not been pointed out in the past. Future work will experimentally evaluate the effectiveness of the proposed method.

References

[1] S. Nandi, S. Ahmed, and H. A. Toliyat, "Detection of rotor slot and other eccentricity related harmonics in a three phase induction motor with different rotor cages," *IEEE Transactions on Energy Conversion*, vol. 16, no. 3, pp. 253–260, 2001.

[2] S. Nandi, H. A. Toliyat, and X. Li, "Condition monitoring and fault diagnosis of electrical motors—a review," *IEEE transactions on energy conversion*, vol. 20, no. 4, pp. 719–729, 2005.

[3] J. Faiz and M. Ojaghi, "Different indexes for eccentricity faults diagnosis in three-phase squirrel-cage induction motors: A review," *Mechatronics*, vol. 19, no. 1, pp. 2–13, 2009.

[4] H. A. Toliyat, S. Nandi, S. Choi, and H. Meshgin-Kelk, *Electric machines: modeling, condition monitoring, and fault diagnosis*. CRC press, 2012.

[5] M. E. H. Benbouzid, "A review of induction motors signature analysis as a medium for faults detection," *IEEE transactions on industrial electronics*, vol. 47, no. 5, pp. 984–993, 2000.

[6] X. Li, Q. Wu, and S. Nandi, "Performance analysis of a three-phase induction machine with inclined static eccentricity," *IEEE Transactions on Industry Applications*, vol. 43, no. 2, pp. 531–541, 2007.

[7] J. Faiz and B. M. Ebrahimi, "Static eccentricity fault diagnosis in an accelerating no-load three-phase saturated squirrel-cage induction motor," *Progress in electromagnetics research*, vol. 10, pp. 35–54, 2008.

[8] M. Akar, "Detection of a static eccentricity fault in a closed loop driven induction motor by using the angular domain order tracking analysis method," *Mechanical Systems and Signal Processing*, vol. 34, no. 1-2, pp. 173–182, 2013.

[9] H. A. Toliyat, M. S. Arefeen, and A. G. Parlos, "A method for dynamic simulation of air-gap eccentricity in induction machines," *IEEE transactions on industry applications*, vol. 32, no. 4, pp. 910–918, 1996.

[10] X. Luo, Y. Liao, H. A. Toliyat, A. El-Antably, and T. A. Lipo, "Multiple coupled circuit modeling of induction machines," *IEEE Transactions on industry applications*, vol. 31, no. 2, pp. 311–318, 1995.

[11] N. A. Al-Nuaim and H. Toliyat, "A novel method for modeling dynamic air-gap eccentricity in synchronous machines based on modified winding function theory," *IEEE Transactions on energy conversion*, vol. 13, no. 2, pp. 156–162, 1998.

[12] A. Sapena-Bano, M. Riera-Guasp, J. Martinez-Roman, M. Pineda-Sanchez, R. Puche-Panadero, and J. Perez-Cruz, "Fem-analytical hybrid model for real time simulation of ims under static eccentricity fault," in *2019 IEEE 12th International Symposium on Diagnostics for Electrical Machines, Power Electronics and Drives (SDEMPED)*. IEEE, 2019, pp. 108–114.